Journal of Materials Science & Technology 109 (2022) 147–156

Contents lists available at ScienceDirect

Journal of Materials Science & Technology

journal homepage: www.elsevier.com/locate/jmst

Heterogeneous GdTbDyCoAl high-entropy alloy with distinctive magnetocaloric effect induced by hydrogenation

Liliang Shao[a], Lin Xue[c], Qiang Luo[a], Kuibo Yin[b], Zirui Yuan[a], Mingyun Zhu[b], Tao Liang[a], Qiaoshi Zeng[d], Litao Sun[b], Baolong Shen[a,*]

[a] School of Materials Science and Engineering, Jiangsu Key Laboratory of Advanced Metallic Materials, Southeast University, Nanjing 211189, China
[b] SEU-FEI Nano-Pico Center, Key Laboratory of MEMS of Ministry of Education, School of Electronic Science and Engineering, Southeast University, Nanjing 210018, China
[c] College of Mechanics and Materials, Hohai University, Nanjing 211100, China
[d] Center for High Pressure Science and Technology Advanced Research, Pudong, Shanghai 201203, China

ARTICLE INFO

Article history:
Received 20 July 2021
Revised 19 August 2021
Accepted 20 August 2021
Available online 2 November 2021

Keywords:
High-entropy metallic glass
Hydrogenation
Heterogeneous structure
Magnetocaloric effect

ABSTRACT

Developing novel magnetocaloric materials is of great significance for the applications of magnetic refrigeration. In this study, we designed a heterogeneous rare-earth-based high-entropy alloy (HEA) comprising amorphous matrix, local crystal-like cluster and nanocrystalline dihydride with average size of 7.5 nm through isothermal hydrogenation. This heterogeneous structure can significantly tune the magnetocaloric effect of alloy. After hydrogenation, the predominant exchange interaction transforms from ferromagnetic to antiferromagnetic with the disappearance of spin-glass-like behavior, and a complete second-order magnetic transition is obtained. Compared with the $Gd_{20}Tb_{18}Dy_{18}Co_{20}Al_{24}$ high-entropy metallic glass with a small number of nanocrystals, the maximum magnetic entropy change of the hydrogen-containing HEA is increased from 8.8 to 13.6 J kg^{-1} K^{-1} under applied magnetic field change of 5 T accompanying unobvious hysteresis and decreased magnetic transition temperature from 59 to 8 K, which is more promising as magnetic refrigerant at cryogenic temperature. This work provides a novel concept of designing heterogeneous structure in terms of special cluster and preferential nanocrystalline to modulate the properties of metallic glasses.

1. Introduction

Magnetic refrigeration based on magnetocaloric effect (MCE) is regarded as the most promising alternative for conventional gas compression refrigeration because of its high energy-efficiency and environmental friendliness [1,2]. In the last decades, magnetocaloric materials have been widely explored, mainly involving crystalline and amorphous materials. For the crystalline materials, giant MCE with large magnetic entropy change (ΔS_M) are often obtained including GdSiGe [3], LaFeSi [4,5], MnFePAs [6], and NiMn-based alloys [7,8], etc. Nevertheless, despite the advantages, several drawbacks due to the first-order nature of magnetic transition, such as the concentrated working temperature interval and undesirable hysteresis, hamper the available cooling capacity of these alloys [9]. Different from the crystalline materials, owning to the topological and chemical disorder, amorphous alloys generally show second-order magnetic transition, exhibiting broadened magnetic transition temperature range with negligible thermal and magnetic hysteresis, but moderate ΔS_M [10]. Recently, high-entropy metallic glasses (HE-MGs) with the advantages of both high-entropy alloy (HEA) and MGs have attracted much attentions [11–16]. Many rare-earth (RE)-based HE-MGs possess obvious MCE such as $Gd_{20}Tb_{20}Dy_{20}Al_{20}M_{20}$ (M = Fe, Co and Ni) [17] and $Er_{20}Dy_{20}Co_{20}Al_{20}RE_{20}$ (RE = Gd, Tb and Tm) [18], providing a new route to design magnetocaloric materials. However, the ΔS_M of RE-based HE-MGs are not large enough. Further increasing the ΔS_M is of importance for their applications.

Hydrogen can penetrate easily into some metals and is often used to improve the magnetic properties of crystalline materials [19,20], for instance, hydrogenation treatment is effective to tune the MCE of $La(Fe,Si)_{13}$-type compounds [21–23]. The interstitial hydrogen expands the lattice and modifies the Fermi level, increasing Curie temperature, while retaining the first-order phase transition intrinsic to the parent intermetallic, and therefore, preserving the large MCE [24]. For example, the peak value of adiabatic temperature change under the maximum applied field of 5 T increases from 8.6 to 12.6 K in the $La(Fe_{0.88}Si_{0.12})_{13}H_{1.5}$ alloy, and the peak

* Corresponding author.
E-mail address: blshen@seu.edu.cn (B. Shen).

https://doi.org/10.1016/j.jmst.2021.08.076
1005-0302/

value of magnetic entropy change ($-\Delta S_M^{peak}$) of $La(Fe_{0.9}Si_{0.1})_{13}H_{1.1}$ alloy at 5 T is larger than 30 J $kg^{-1}K^{-1}$ [22]. The REs can also absorb hydrogen readily and form solid solutions, dihydride β-phase and/or trihydride γ-phase, which not only directly influence the Ruderman-Kittel-Kasuya-Yosida (RKKY) interaction responsible for the magnetism, but also leads to modifications of the crystal-field symmetry [19]. Therefore, hydrogenation plays a significant role in modulating the MCE of REs [25]. Beside, based on a modified hydrogenation disproportionation desorption recombination process, anisotropic nano-composite NdFeB/α-Fe magnet powders with enhanced maximum energy product are synthesized [26]. This means hydrogenation is supposed to decrease the magnetic hysteresis that is an important parameter for MCE. However, minor investigation involved the effects of hydrogenation on MCE of RE-based HE-MGs have been reported. Molecular dynamics simulations indicate that hydrogenation can promote the formation of hydrogen-containing clusters, overcoming the strength-toughness trade-off of ZrCu-based MGs [27]. In a DyCoAl MG, hydrogenation is found to improve the ΔS_M because of the expansion of average interatomic distance [28], whereas ΔS_M decrease slightly after hydrogenation in a GdCoAl MG [29]. Therefore, whether hydrogenation can enhance the ΔS_M of pure MG is uncertain. Due to the sluggish diffusion effect of HEAs, HE-MGs in the same alloy system usually exhibit higher stability against crystallization upon heating [11], which guarantees the controllable crystallization during long-term annealing. Inspired by these, we performed isothermal hydrogenation to enhance the heterogeneity of RE-based HE-MGs and obtain uniformly distributed-nanocrystals with appropriate size with the expectation of increasing ΔS_M, which has not been investigated systematically.

In this work, a $Gd_{20}Tb_{18}Dy_{18}Co_{20}Al_{24}$ high-entropy bulk metallic glass (BMG) with good glass-forming ability and typical MCE was designed, and heterogeneous structures composed of amorphous matrix, local-favored clusters and nanocrystalline dihydrides were obtained through isothermal hydrogenation below the glass transition temperature (T_g) of HE-BMG. This hydrogen-induced heterogeneous HEA showed distinctive magnetocaloric property and magnetic transition compared with the hydrogen-free alloy.

2. Experimental methods

Master alloy of $Gd_{20}Tb_{18}Dy_{18}Co_{20}Al_{24}$ was prepared by arc-melting a mixture of pure Gd, Tb, Dy, Co and Al in a titanium-gettered argon atmosphere. The purities of Gd, Tb and Dy elements are better than 99.9 wt.% and those of Co and Al elements are better than 99.99 wt.%. The BMG samples with diameter of 2 mm were fabricated by copper mold casting, then mechanical ball-milling was used to prepare amorphous powders with particle size less than 200 meshes. The T_g of prepared amorphous powders was identified as 606 K using differential scanning calorimetry (DSC, Netzsch DSC 404 F3) at the heating rate of 20 K/min. The isothermal hydrogenation experiment was performed on a Sieverts-type apparatus (Advanced Materials Corporation, No. 0360Q).

Temperature and field dependences of the DC magnetization were measured using a SQUID magnetometer (MPMS, Quantum Design). The field cooling (*FC*) magnetization was measured on the heating course after initial cooling from room temperature to 2 K, with an applied magnetic field of 0.01 T. The zero-field cooling (*ZFC*) magnetization was measured on the heating course under the same magnetic field after initial cooling the sample from room temperature to 2 K with zero field. Isothermal magnetization curves were measured with a varying magnetic field increasing from 0 to 5 T at different temperatures ranging from 10 to 120 K. AC susceptibility was measured at frequencies ranging from 13 to 9673 Hz with amplitude of 5 Oe using a physical properties measurement system (PPMS 6000, Quantum Design).

The structures of powders were examined by X-ray diffraction (XRD, Rigaku SmartLab 9 K) using Cu-Kα radiation. The morphology and size distribution were characterized by scanning electron microscopy (SEM, FEI Sirion 200). Furthermore, the structural features at nanoscale were investigated by spherical aberration-corrected transmission electron microscopy (TEM, Titan 80–300). Focused ion beam (FIB, FEI Scios) was used to prepare the TEM samples. The thickness of the detected regions for the two HRTEM foils was estimated to be 19 ± 1 nm by electron energy loss spectroscopy. The nanoindentation tests were conducted using a NanoTest Vantage (Micro Materials Ltd) with a standard Berkovich diamond indenter in load control mode. Starting with a linear ramp up to the maximum load of 10 mN within 10 s, the loading course was continued by holding the maximum load for 10 s, and finally by unloading to zero.

3. Results and discussion

3.1. Isothermal hydrogenation

The $Gd_{20}Tb_{18}Dy_{18}Co_{20}Al_{24}$ alloy possesses good glass-forming ability and can be easily prepared into BMG sample with the diameter of 3 mm, which guarantees the subsequent ball-milling treatment. Fig. 1(a) shows the SEM image of $Gd_{20}Tb_{18}Dy_{18}Co_{20}Al_{24}$ powders with an average diameter of 41 ± 1.6 μm prepared by mechanical ball-milling. The subsequent hydrogenation, magnetic measurements, TEM observation and nanoindentation test were all performed using theses powders. Isothermal hydrogenation was performed at the temperature of 538 K far below T_g. Before isothermal hydrogenation, the hydrogen pressure was set as 5 MPa. After annealing for 1.5×10^5 s, the hydrogen content was calculated to be 1.2 wt.% by the apparatus according to the decrease of pressure. Thus, the chemical formula of the hydrogen-containing sample can be written as $(Gd_{0.2}Tb_{0.18}Dy_{0.18}Co_{0.2}Al_{0.24})_{43}H_{57}$. For comparison, the $Gd_{20}Tb_{18}Dy_{18}Co_{20}Al_{24}$ powders were also annealed at 538 K for 1.5×10^5 s with the hydrogen pressure of 0 MPa. Corresponding XRD patterns of the $Gd_{20}Tb_{18}Dy_{18}Co_{20}Al_{24}$ (GdTbDyCoAl) and $(Gd_{0.2}Tb_{0.18}Dy_{0.18}Co_{0.2}Al_{0.24})_{43}H_{57}$ (GdTbDyCoAlH) powders are shown in Fig. 1(b). Several inconspicuous crystalline peaks are detected for the GdTbDyCoAl powders, implying that a small number of nanocrystals including Al_3Dy, $TbAl_3$, Al_2Gd_3 and $CoGd_3$ precipitate in the amorphous matrix after long-term annealing treatment below T_g. It is found that some REH_2 phases precipitate and the crystalline peaks become more distinct after hydrogenation. Beside, the major amorphous hump shifts to lower angle, which is consistent with the previous reports [28,30] and indicates the expansion of average interatomic distance.

3.2. Magnetocaloric property

It can be expected that the structural changes induced by hydrogen will alter the magnetocaloric properties of the studied HE-MGs. To evaluate the magnetocaloric property, isothermal magnetization curves (M–H) were measured as shown in Fig. 2(a) and (b). With the increase of field, both samples magnetize to saturation gradually showing ferromagnetic feature. Beside, a clear magnetic transition from magnetic order to magnetic disorder with increasing temperature can be seen. Subsequently, ΔS_M was calculated using Eq. (1) based on the M–H curves [31].

$$\Delta S_M(T,H) = \int_0^{H_{max}} \left(\frac{\partial M}{\partial T}\right)_H dH \quad (1)$$

where H_{max} is the maximum applied magnetic field. Fig. 3(a) and (b) exhibits the temperature dependent ΔS_M under a series of applied fields. It can be seen that $-\Delta S_M^{peak}$ for the GdTbDyCoAl sam-

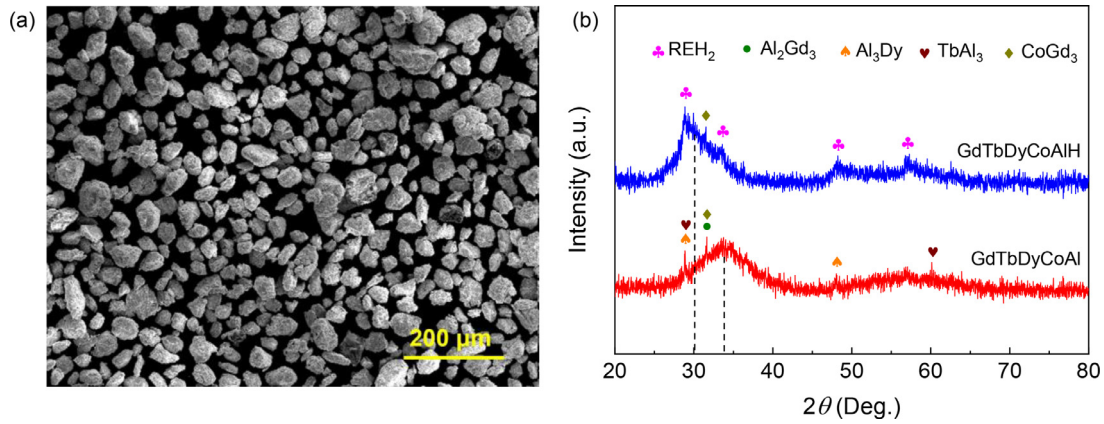

Fig. 1. (a) SEM image of the $Gd_{20}Tb_{18}Dy_{18}Co_{20}Al_{24}$ amorphous powders. (b) XRD patterns of the GdTbDyCoAl and GdTbDyCoAlH powders.

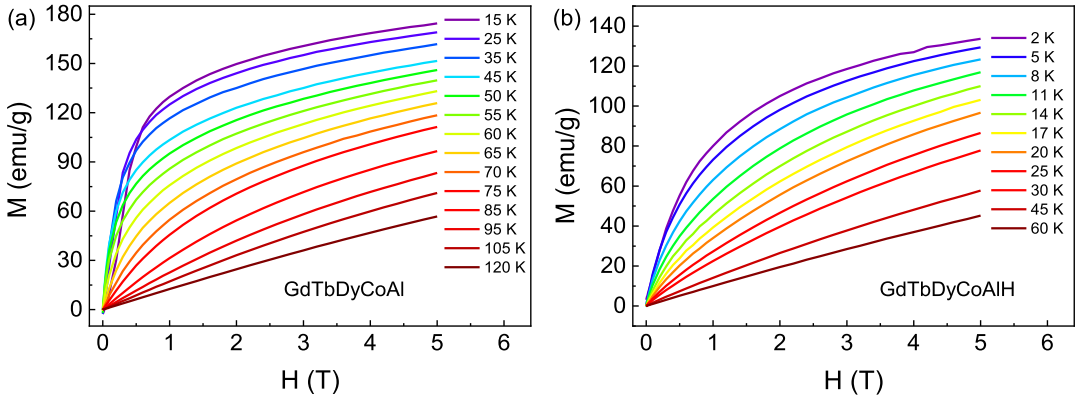

Fig. 2. Isothermal magnetization curves for the (a) GdTbDyCoAl and (b) GdTbDyCoAlH powders.

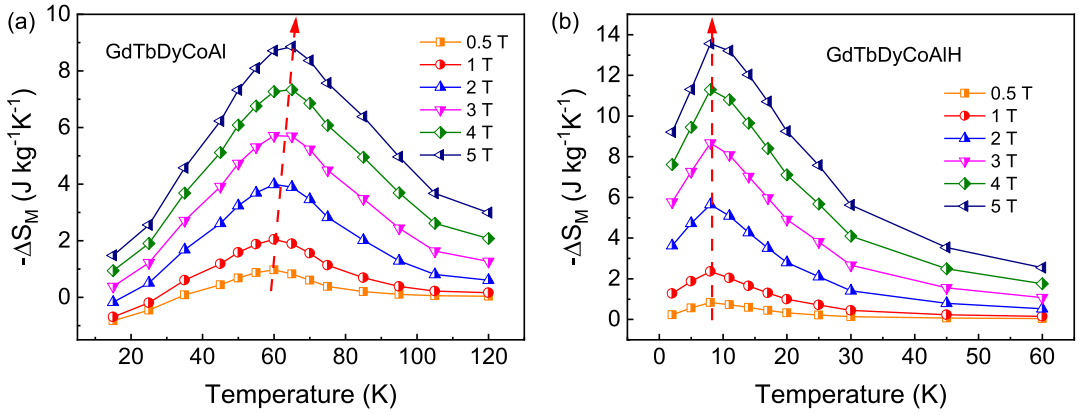

Fig. 3. Temperature dependence of ΔS_M under the maximum applied field from 0.5 to 5 T for the (a) GdTbDyCoAl and (b) GdTbDyCoAlH powders.

ple increases gradually and moves to higher temperature with the applied field increasing from 0.5 to 5 T. However, for the GdTbDyCoAlH sample, the peak temperature does not change with the variation of applied field and locates at 8 K. In particular, the value of $-\Delta S_M^{peak}$ at the maximum magnetic field of 5 T increases from 8.8 to 13.6 J $kg^{-1}K^{-1}$ after absorbing hydrogen, which is larger than the values of most reported HE-MGs and comparable to those of the crystalline magnetocaloric materials exhibiting similar magnetic transition temperature (e.g. the $-\Delta S_M^{peak}$ at 5 T for the Tm_4PdMg, $HoNiAl_2$ and Ho_2ZnMnO_6 compounds are 14.9, 14.0 and 13.2 J $kg^{-1}K^{-1}$, respectively) [32–34].

The field dependence of ΔS_M follows a power law of $\Delta S_M \propto H^n$ with an exponent (n) depending on field and temperature [35]. Fig. 4(a) and (b) shows the calculation of n for the GdTbDyCoAl and GdTbDyCoAlH samples, respectively. It is seen that the field dependent ΔS_M at low temperatures cannot be described by the power law for the GdTbDyCoAl sample as shown in Fig. 4(a), implying strong random magnetic anisotropy (RMA). The variations of n are plotted in Fig. 4(c), and the temperature axis is rescaled by subtracting magnetic transition temperature (T_M). According to mean field theory, the n value has a minimum of 2/3 at T_M [35]. However, the minimum n values are 0.89 and 1.02 for GdTbDyCoAl and GdTbDyCoAlH, respectively, larger than the predicated value. The value of n is sensitive to atomic/magnetic structure and details of transition process [30]. In the GdTbDyCoAl sample, large RMA is introduced by Tb and Dy elements, and Gd element pos-

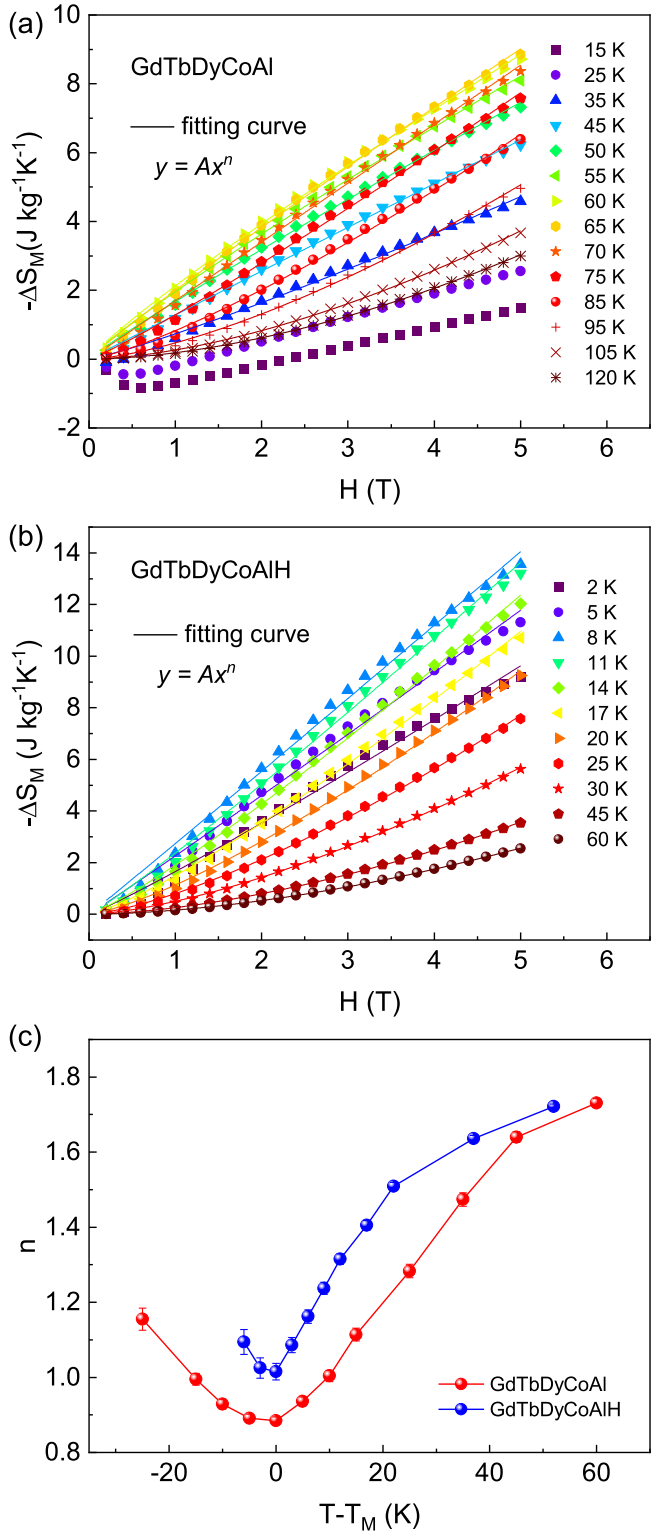

Fig. 4. Field dependence of ΔS_M at different temperatures for the (a) GdTbDyCoAl and (b) GdTbDyCoAlH powders. (c) Temperature dependence of n values obtained from (a) and (b).

sesses strong exchange interaction. The competition between RMA and exchange interactions leads to a complex magnetic structure [36]. Beside, a few nanocrystals precipitate after annealing. The combined effects of these two aspects result in the large n value of GdTbDyCoAl sample. With the absorption of hydrogen, multiple magnetic phases including amorphous matrix and a large number of nanocrystalline dihydrides contribute to a larger n value, which means an easier enhancement of ΔS_M by increasing applied field. Therefore, hydrogenation can not only increase the value of $-\Delta S_M^{peak}$ but also raise the sensitivity of ΔS_M to field. It is noteworthy that there seems to be a "paradox" that hydrogenation results in obvious decrease of magnetization as shown in Fig. 2 and large increase of ΔS_M in Fig. 3. This can be elucidated from the definition of ΔS_M, Eq. (1). At a given field change, ΔS_M depends on the change rate of magnetization with increasing temperature. That is to say the value of ΔS_M is not only decided by the number of magnetic moment but also the moving speed of magnetic moment. If a great number of magnetic moments rotate rapidly near T_M, the sample will possess large ΔS_M. As can be seen from Fig. 3, the temperature span of magnetic transition decreases obviously after hydrogenation, i.e., the motion of magnetic moment during magnetic transition becomes faster, leading to a larger ΔS_M. This can also be proved by the larger value of n for the hydrogen-containing sample as shown in Fig. 4(c).

Another important index for the application of magnetocaloric materials is magnetic hysteresis. As shown in Fig. 5(a), the hysteresis loops at 5 K for the two samples were measured. Both the coercivity and saturation magnetization decrease obviously after hydrogenation, leading to a much smaller magnetic hysteresis. Subsequently, the magnetizing and demagnetizing M–H curves at several temperatures were measured as shown in Fig. 5(b) and (c) for the two samples. At low temperatures (5 and 15 K), the magnetizing and demagnetizing curves cannot overlap and there is significant hysteresis for the GdTbDyCoAl sample. The hysteretic loss was determined by calculating the area inside each M–H loop as summarized in Fig. 5(d). As the temperature increases to T_M, hysteretic loss reduces sharply to near zero because of the repaid decrease in RMA [37]. Although the variation of hysteresis for the GdTbDyCoAlH sample is analogous to this as displayed in the inset of Fig. 5(d), the value of hysteretic loss is much smaller than that of the GdTbDyCoAl sample at relatively low temperature, and the two M-H curves nearly superpose together with little hysteresis at all temperatures. Therefore, both the studied two HEAs possess negligible hysteresis during magnetic transition near T_M, which is more suitable for using as magnetic refrigerant [2], and hydrogenation can reduce hysteretic loss at cryogenic temperature. Generally, hysteresis and ΔS_M correlate with magnetic transition. Thus, the magnetic transition is altered by hydrogenation.

3.3. Magnetic transition

To identify the nature of magnetic order for the studied HEAs, M–H data were further analyzed by transferring to Arrott plots as shown in Fig. 6(a) and (b). For the GdTbDyCoAl sample, curves show negative slope at low temperatures and low applied fields, consisting with the intersection of magnetization curves in Fig. 2(a), whereas only positive slope occurs for the GdTbDyCoAlH sample. This means that a complete second-order magnetic transition is obtained after hydrogenation [38]. It has been demonstrated that the ΔS_M curves for magnetocaloric materials with second-order transition can collapse into a universal curve [39]. Fig. 6(c) and (d) displays the universal curves of the GdTbDyCoAl and GdTbDyCoAlH samples, respectively. The temperature axis is rescaled using a single parameter formula as follow:

$$\theta = (T - T_p)/(T_r - T_p) \quad (2)$$

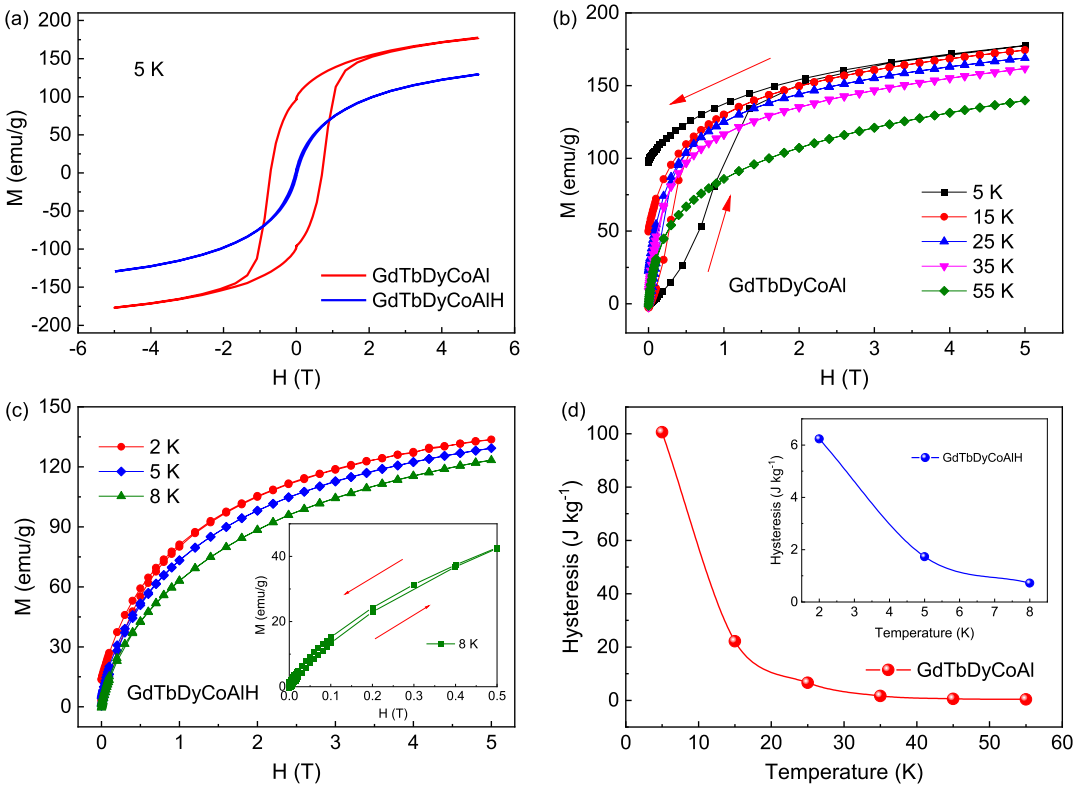

Fig. 5. (a) Magnetic hysteresis loops from -5 to 5 T at the temperature of 5 K for the two samples. Isothermal magnetizing and demagnetizing *M–H* curves at several temperatures below T_M for the (b) GdTbDyCoAl and (c) GdTbDyCoAlH samples. (d) Temperature dependence of hysteretic loss.

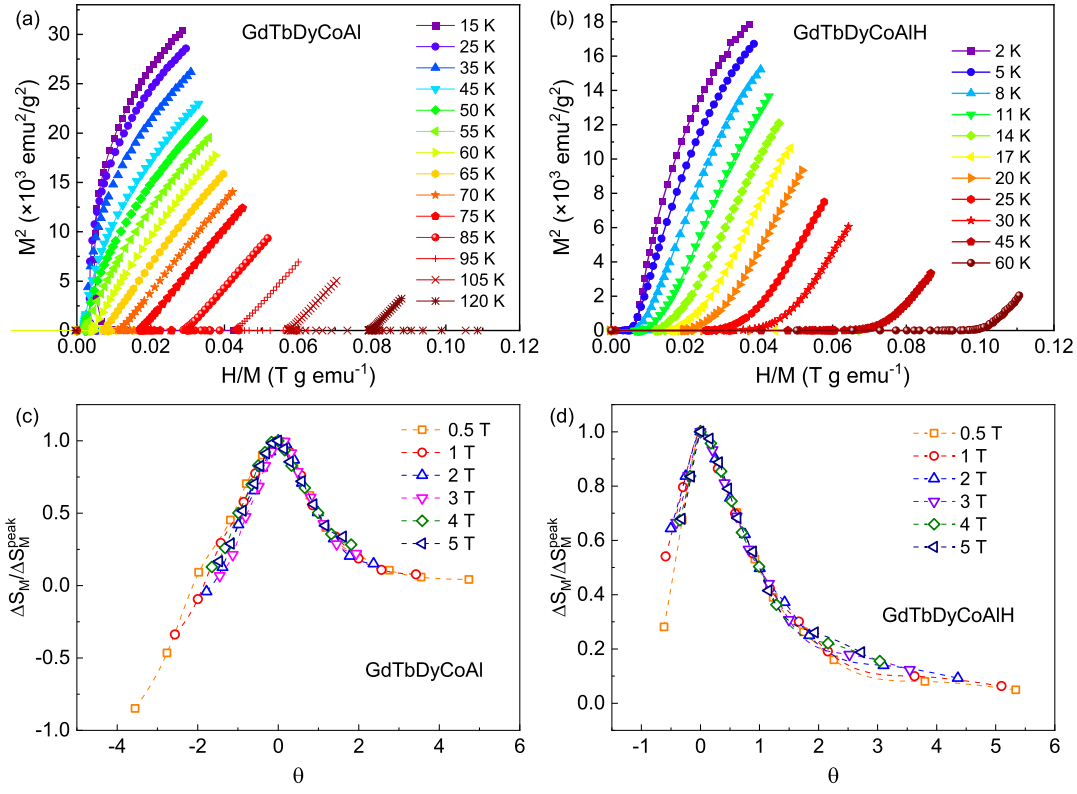

Fig. 6. Arrott plots calculated from *M–H* curves for the (a) GdTbDyCoAl and (b) GdTbDyCoAlH powders. (c) and (d) The universal curves of ΔS_M for the samples.

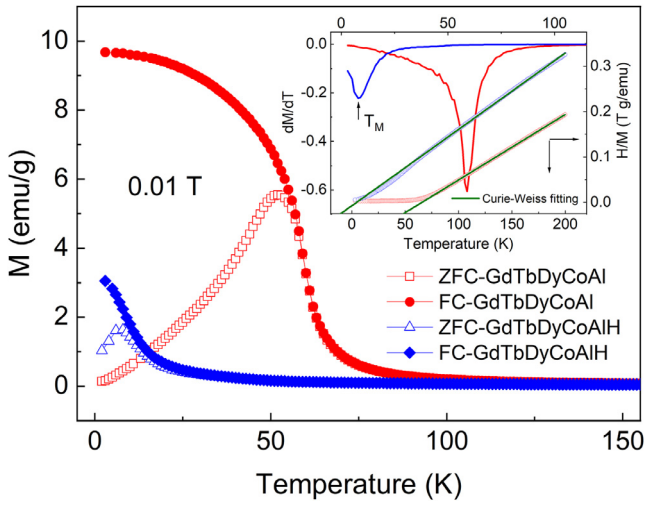

Fig. 7. Temperature dependence of magnetization under the applied magnetic field of 0.01 T for the GdTbDyCoAl and GdTbDyCoAlH powders. The inset shows the determination of T_M and Curie-Weiss fitting.

where T_p is the peak temperature of ΔS_M curves and T_r is the reference temperature with $\Delta S_M(T_r) = 0.5\Delta S_M^{peak}$. It can be seen that the normalization curves under different applied fields overlap well near the peak temperature ($-1 \le \theta \le 1$) for both samples, confirming a second order transition occurred in T_M. For the GdTbDyCoAl sample, the universal curves cannot overlap and large negative values of $\Delta S_M/\Delta S_M^{peak}$ appear attributed to the strong RMA at low temperatures and fields. Different from this, no negative values can be seen for the GdTbDyCoAlH sample, and the mismatch of universal curves results from the multiple magnetic phases [40], i.e., the dihydrides induced by hydrogen.

The temperature dependence of magnetization (M–T) curves were used to further investigate magnetic transition as shown in Fig. 7. It is seen that with the decrease of temperature the GdTbDyCoAl sample firstly undergoes paramagnetic to ferromagnetic transition at the temperature of 59 K due to the magnetic ordering. Then it enters a spin-glass (SG)-like state below 51 K showing a divergence between *FC* and *ZFC* curves. This causes the presence of temperature-dependent coercivity and is interpreted as the random freezing of the magnetic moments along local anisotropy axes due to spin orbit coupling. Owing to the coexistence of multi-principle RE elements including Gd, Tb and Dy, the competition between RMA and exchange interaction results in the frustration of SG transition, i.e., a gradual transition below the freezing temperature [36]. Compared with the hydrogen-free sample, the magnetization and magnetic ordering transition temperature (T_M) decrease dramatically after hydrogenation. As shown in the insert of Fig. 7, the value of T_M is determined by the differential of *FC* magnetization curve, decreasing from 59 to 8 K after hydrogenation, identical to the value obtained from ΔS_M curves. According to the anionic model [41], electrons can transfer from the conduction band to the hydrogen 1 s shell upon hydrogenation, resulting in a reduction of the electrons available to mediate the RKKY indirect interaction, and thus T_M decreases obviously. Furthermore, the divergence between *FC* and *ZFC* curves for the GdTbDyCoAlH sample is inconspicuous, indicating a different magnetic transition at low temperature. The Curie-Weiss fits (shown in the inset) of M–T data demonstrate that the paramagnetic Curie temperature changes from positive (48 K) for the GdTbDyCoAl sample to negative (-9 K) for the GdTbDyCoAlH sample. This means that the predominant exchange interaction transforms from ferromagnetic to antiferromagnetic after hydrogenation, hence the *ZFC* curve shows a cup near 7 K. Owing to the remnant of ferromagnetic phases including some amorphous phase and hydrogen-free nanocrystals, *FC* curve still increases gradually below T_M, leading to the divergence between *ZFC* and *FC* curves for the GdTbDyCoAlH sample.

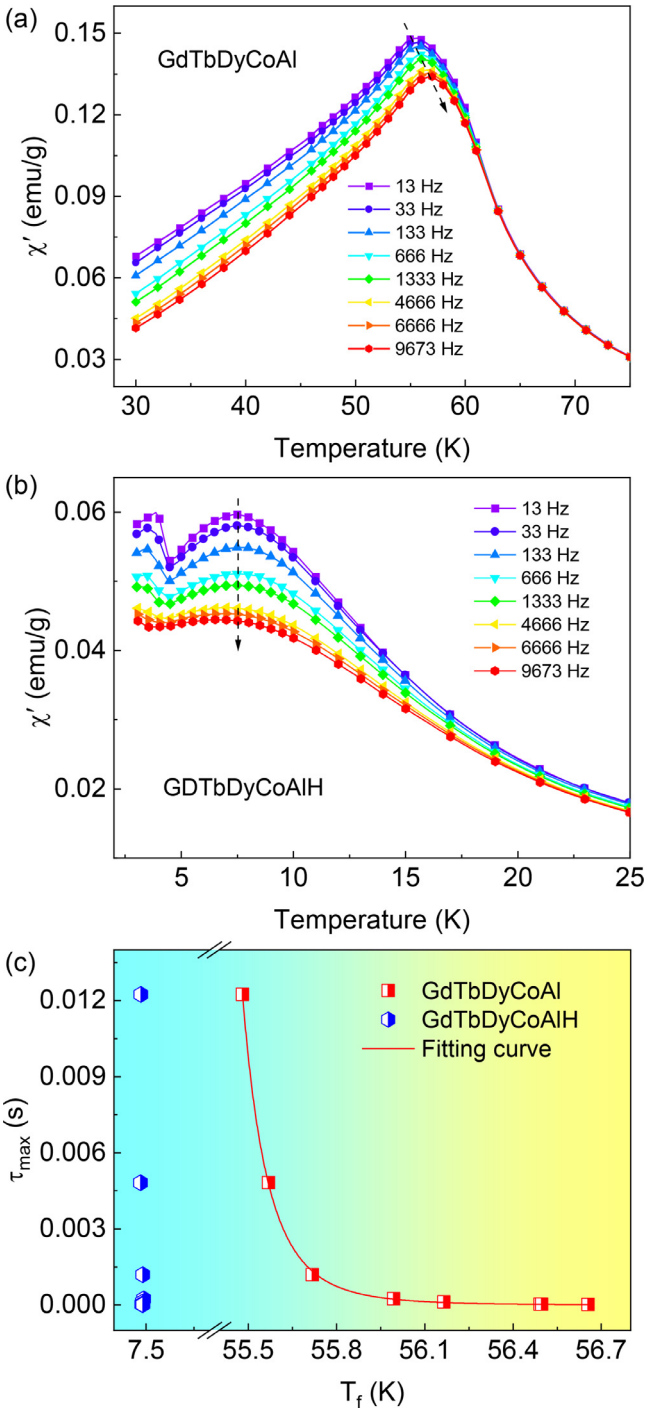

Fig. 8. The real part of susceptibility (χ') at frequency ranging from 13 to 9673 Hz for the (a) GdTbDyCoAl and (b) GdTbDyCoAlH samples. (c) The maximum relaxation time (τ_{max}) versus the peak temperature of susceptibility (T_f) for the samples.

To characterize the critical dynamics of the magnetic transition, AC susceptibilities at different frequencies were measured as displayed in Fig. 8(a) and (b). For the GdTbDyCoAl sample, the real part of susceptibility (χ') exhibits a peak at the temperature lower than T_M, and the value of the peak (T_f) shifts to higher temperature with increasing frequency. The relative shift in freezing temperature (δT_f) per decade of frequency is often used to compare differ-

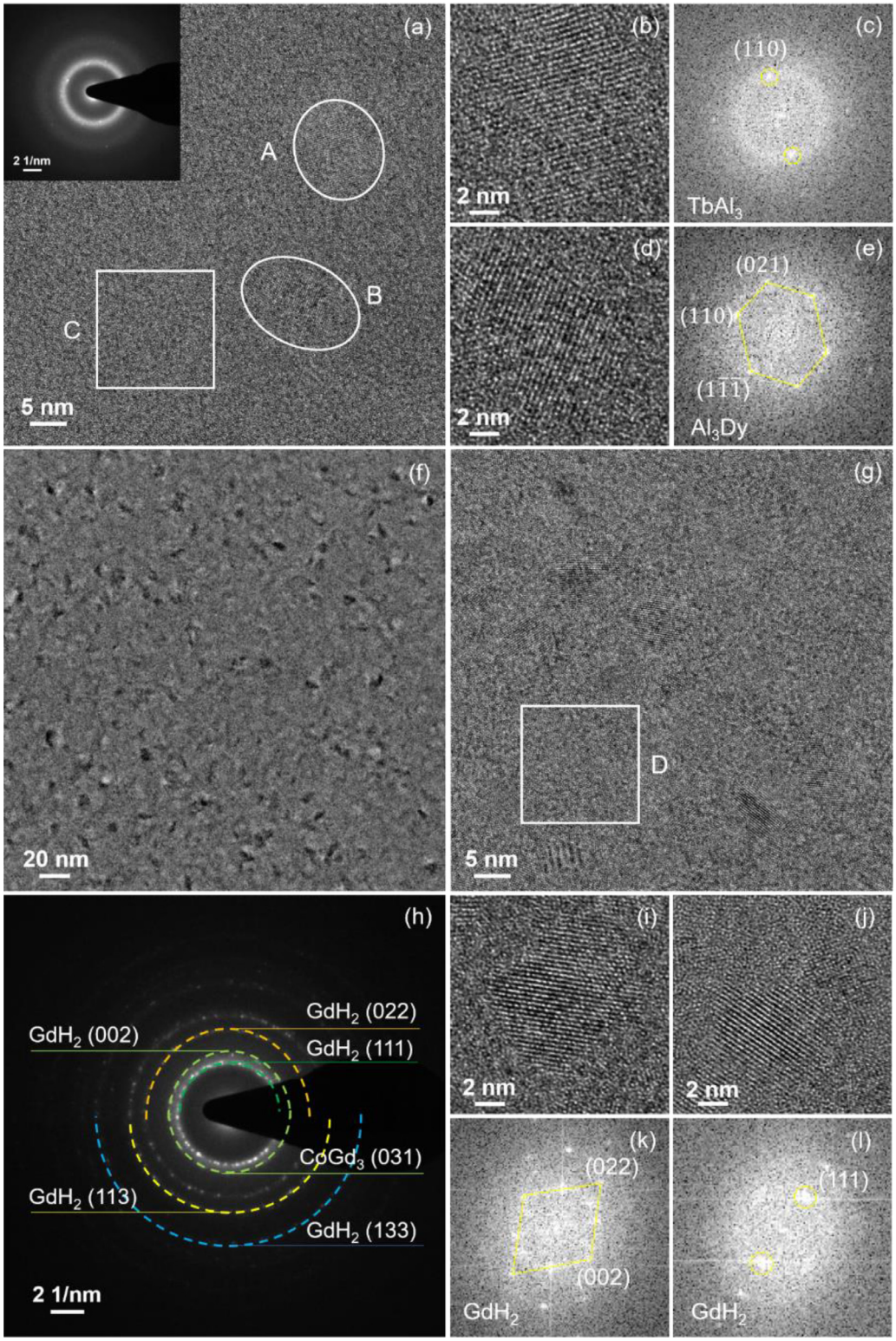

Fig. 9. HRTEM images and corresponding FFT patterns for (a)–(e) GdTbDyCoAl and (f)–(l) GdTbDyCoAlH samples, respectively.

ent SG systems. This parameter of GdTbDyCoAl was calculated by the following relation [42]:

$$\delta T_f = \frac{\Delta T_f}{T_f \Delta(\log_{10}\nu)} \tag{3}$$

where $\Delta T_f = (T_f)_{\upsilon_1} - (T_f)_{\upsilon_2}$ and $\Delta(\log_{10}\upsilon) = \log_{10}\upsilon_1 - \log_{10}\upsilon_2$. In this study, ν_1 = 33 Hz, ν_2 = 9673 Hz and $T_f = (T_f)_{\upsilon_1}$ were employed. The value of δT_f is 0.0079, which is in the same order of magnitude with the values reported for canonical SG systems [42]. Different from this, the peak of GdTbDyCoAlH becomes much broader, and T_f does not show obvious change at various frequencies. For a critical slowing down of dynamics, the correlation length diverges at the transition temperature and the relaxation time ($\tau_{max} = 1/\omega$) obeys the power law as follow [43]:

$$\tau_{max} = \tau_0 \times (T_f/T_{sg} - 1)^{-z\nu} \tag{4}$$

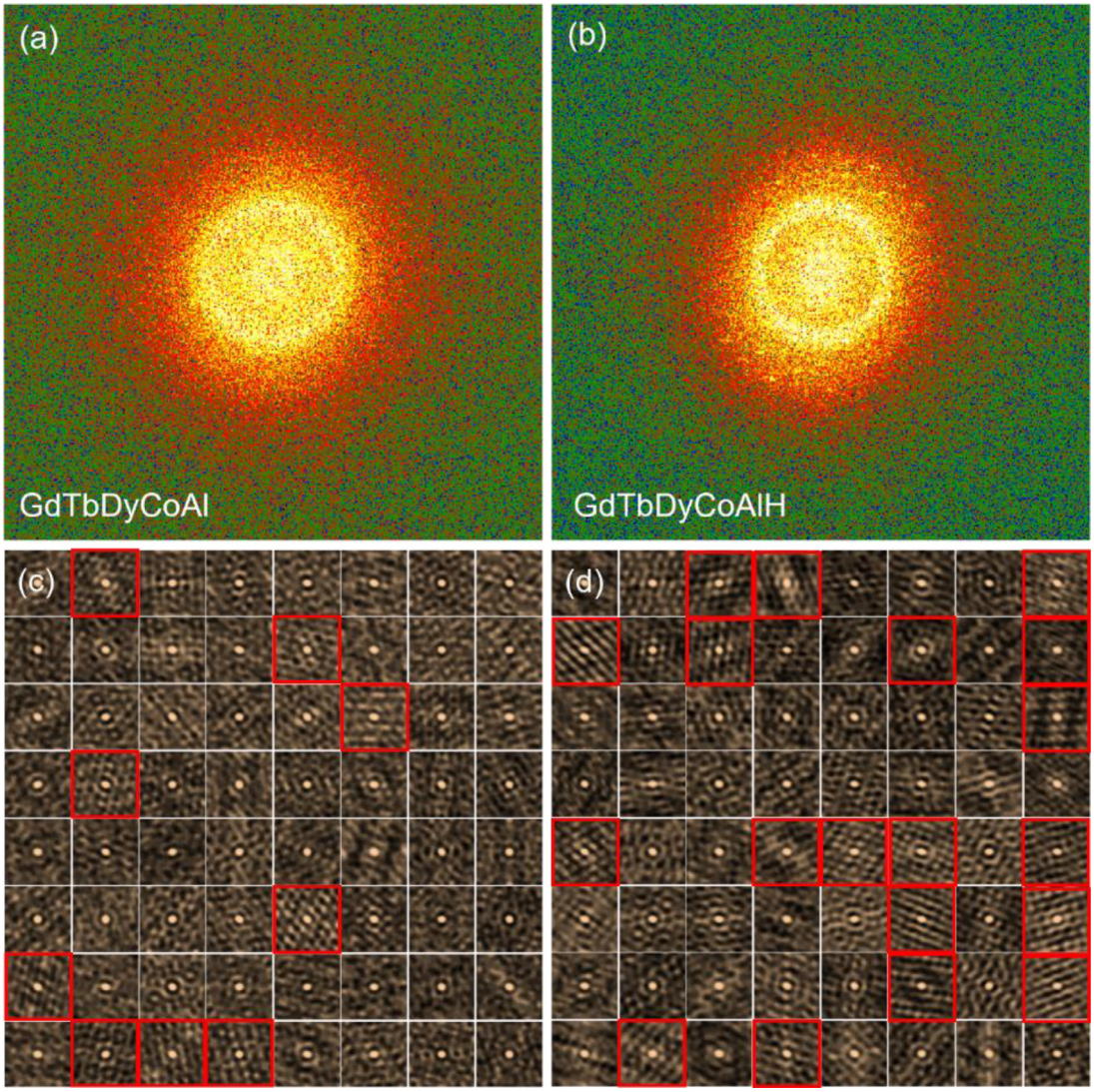

Fig. 10. FFT patterns of the selected areas (C and D) in Fig. 9(a) and (g) for the (a) GdTbDyCoAl and (b) GdTbDyCoAlH samples. (c) and (d) showing the corresponding segmentation of the HRTEM image for auto-correlation analysis. The dimension of each cell is 1.98 × 1.98 nm^2.

where T_{sg} and zv are the ideal freezing temperature and a critical exponent, respectively, and τ_0 is related to the relaxation time of individual atomic magnetic moment. For the typical SG system, τ_0 and zv are in the range of 10^{-10}–10^{-13} and 4–13, respectively [44]. As shown in Fig. 8(c), τ_{max} of the GdTbDyCoAl sample decreases sharply at the initial stage and then tends to zero gradually with the increase of T_f from 55.50 to 56.66 K, and Eq. (4) is used to fit the plots. τ_0 and zv are 1.9 × 10^{-13} and 5.2, respectively, which are in the characteristic range of canonical SG. However, for the GdTbDyCoAlH sample, τ_{max} decreases at a constant T_f ~7.49 K, indicating that the hydrogen-doped sample is not a SG system, which is consistent with the antiferromagnetism identified by *M–T* curve and further verified that the divergence between *ZFC* and *FC* curves for GdTbDyCoAlH sample results from the coexistence of antiferromagnetic and ferromagnetic phases at cryogenic temperature. The distinctive MCE and magnetic transition after hydrogenation are supposed to originate obvious changes of microstructure, which can be reflected preliminarily by XRD. In the following section, systematic characterizations of structures at nanoscale and microscale were performed.

3.4. Heterogeneous structure induced by hydrogenation

Fig. 9(a) shows the high-resolution (HR) TEM image and the selected area electron diffraction (SAED) pattern of the GdTbDyCoAl sample. Two local crystalline regions with a size of ~10 nm can be seen, whereas most of the regions show amorphous structure with random atomic arrangement. This is confirmed by the SAED pattern exhibiting halo-like feature with several bright spots. The magnifications of regions A and B and corresponding fast Fourier transformed (FFT) patterns are exhibited in Fig. 9(b)–(e), respectively. The detected two crystalline phases are identified as $TbAl_3$ and Al_3Dy, consisting with the XRD analyses. Different from the hydrogen-free sample, considerable crystalline particles with average size of 7.5 ± 0.23 nm distribute uniformly in the amorphous matrix after hydrogenation as shown in Fig. 9(f). The HRTEM image of the GdTbDyCoAlH sample is displayed in Fig. 9(g). Numerous nanocrystals with different orientations can be clearly observed. It is noteworthy that four apparent crystalline peaks corresponding to REH_2 phases exist in the XRD patterns of the GdTbDyCoAlH powders as shown in Fig. 1(b), which is confirmed by SAED analyses. As shown in Fig. 9(h), several diffraction rings corresponding

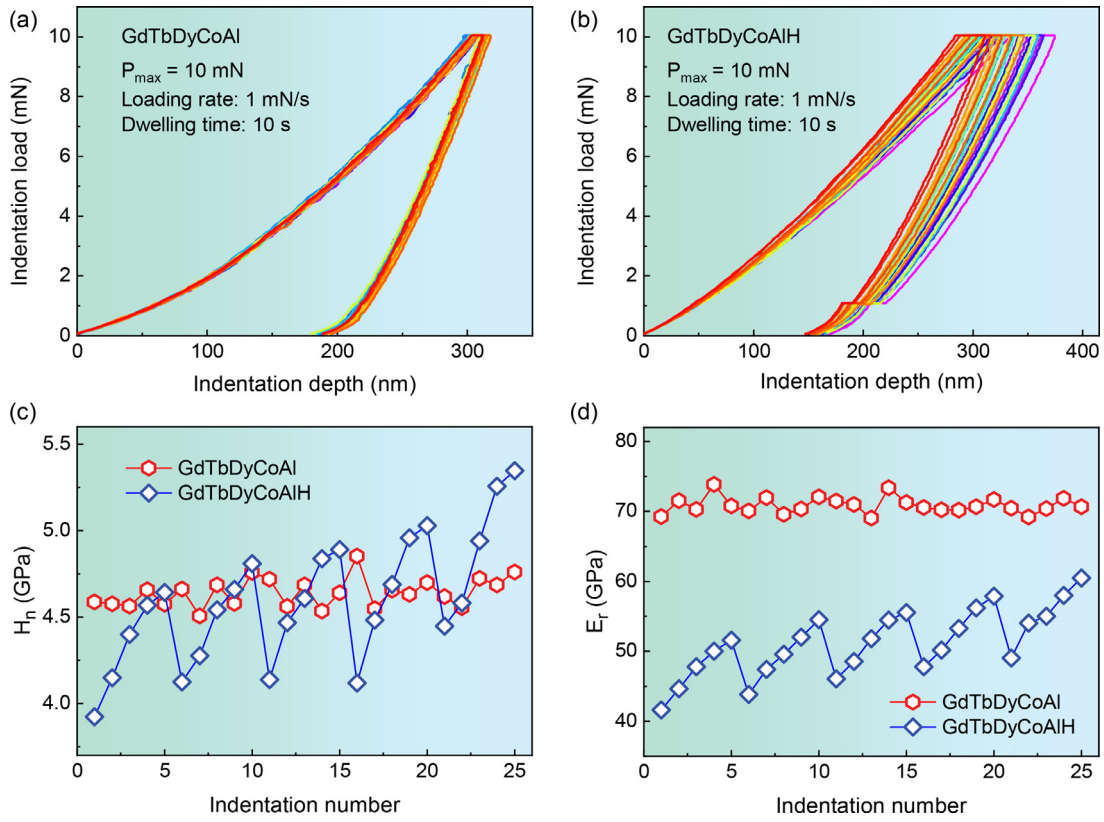

Fig. 11. Indentation load versus indentation depth of the 5 × 5 array for the (a) GdTbDyCoAl and (b) GdTbDyCoAlH powders, respectively. (c) and (d) Variations of the hardness (H_n) and reduced modulus (E_r) obtained from the nanoindentation tests for the GdTbDyCoAl and GdTbDyCoAlH samples.

to GdH_2 phases with different orientations can be seen. Two representative HRTEM images of GdH_2 phases with clear lattice fringe and the related FFT patterns are presented in Fig. 9(i)–(l), respectively.

It was reported that microalloying elements that possess large negative enthalpy of mixing with principal components can increase the number of local crystal-like cluster [45–47]. Hydrogen has large negative enthalpy of mixing with Gd, Tb and Dy elements (-61 kJ/mol), hence it is supposed to promote the formation of local orders. Fig. 10(a) and (b) shows the diffraction patterns of the regions C and D in Fig. 9(a) and (g), and the typical halo-like patterns identify their overall amorphous structure. To study the effect of hydrogen on the amorphous matrix, auto-correlation analyses of regions C and D were carried out and the corresponding mappings are exhibited in Fig. 10(c) and (d). The details of auto-correlation analysis were described in Ref. [47]. The total fraction of the crystal-like cluster is 14.1% in the hydrogen-free sample. By comparison, the areal fraction increases to 29.7% in the hydrogen-containing sample. Therefore, the introduction of hydrogen results in a more heterogeneous microstructure comprising amorphous matrix, local crystal-like clusters and considerable nanocrystalline phases. This heterogeneous structure is supposed to have some significant influences on microscale heterogeneity of HEA.

Subsequently, the nanoindentation test was conducted to investigate the difference of microscale heterogeneity caused by hydrogen. The load-displacement (P–h) curves of GdTbDyCoAl and GdTbDyCoAlH powders collecting from 25 different points (5 × 5 array) are exhibited in Fig. 11(a) and (b), respectively, where P is loading force and h is the instantaneous indenter displacement. It is seen that curves coincide well with each other for the GdTbDyCoAl sample, while those for the GdTbDyCoAlH sample are discrete. The variations in hardness (H_n) and reduced elastic modulus (E_r) obtained from the nanoindentation tests are shown in Fig. 11(c) and (d), respectively. Different from the GdTbDyCoAl sample where the H_n varying between 4.51 and 4.85 GPa with an average value of 4.46 ± 0.09 GPa, the fluctuation value of H_n for the GdTbDyCoAlH sample is 1.43 GPa with a slightly larger average hardness of 4.60 ± 0.36 GPa. The average E_r of the GdTbDyCoAl sample is 68.15 ± 1.16 GPa and the change is 4.88 GPa, whereas the corresponding values for the GdTbDyCoAlH sample are 51.25 ± 4.74 GPa and 18.90 GPa. Accordingly, the distributions of H_n and E_r fluctuate more significantly after hydrogenation, which means the heterogeneity at microscale is also enhanced in the GdTbDyCoAlH sample.

The above results indicate that heterogeneous RE-based HEA is obtained by isothermal hydrogenation, and the heterogeneous structure has significant effects on the magnetocaloric properties and magnetic transition of HEA, i.e., increasing ΔS_M and transforming the magnetic transition from ferromagnetic-paramagnetic to antiferromagnetic-paramagnetic. This can be elucidated from a combination of the flowing aspects. Firstly, hydrogenation induces the expansion of average interatomic distance and promotes the formation of locally favored clusters in the amorphous matrix [30,48], in this study, which are identified as crystal-like clusters. The increasement of local clusters can enhance the ΔS_M to a certain extent [49]. Secondly, the magnetic transition temperatures of the dihydride β-REH_2 phases are 21, 17 and 3.5 K for Gd, Tb and Dy [25], respectively, which are lower than that of GdTbDyCoAl HE-MG (59 K), resulting in the dramatic decrease of T_M. Thirdly, the precipitation of nanocrystals can tune the Fermi surface and the crystal-field symmetry [19], leading to a change of the exchange interactions between magnetic moments. In this study, hydrogen suppresses indirect RKKY exchange interaction and reduces

the RMA at cryogenic temperature. Therefore, the motion of magnetic moment is easier with increasing temperature and applied field, leading to the transformation from ferromagnetic to antiferromagnetic as well as larger ΔS_M and n.

4. Conclusion

In summary, we designed a quinary $Gd_{20}Tb_{18}Dy_{18}Co_{20}Al_{24}$ HE-BMG and obtained a heterogeneous $(Gd_{0.2}Tb_{0.18}Dy_{0.18}Co_{0.2}Al_{0.24})_{43}H_{57}$ HEA through isothermal hydrogenation. Hydrogen promotes the formation of local crystal-like cluster, leading to the enhancement of heterogeneity of amorphous matrix. Beside, more nanocrystalline phases including dihydride and hydrogen-free nanocrystals precipitate in the hydrogen-containing sample. Thus, a more heterogeneous structure at nanoscale is induced by hydrogenation, which contributes to the microscale heterogeneity manifesting as more fluctuant distributions of hardness and modulus. Due to the synergistic effects of heterogeneous structures, the cryogenic magnetism is tuned from ferromagnet to antiferromagnet with T_M decreasing from 59 of 8 K, and the GdTbDyCoAlH HEA shows good MCE with larger $-\Delta S_M^{peak}$ of 13.6 J $kg^{-1}K^{-1}$ under the maximum applied field of 5 T and unobvious hysteresis at the whole temperature span. This new heterogeneous HEA, with the exceptional properties promising for magnetic refrigeration, provides a paradigm to design the next-generation magnetocaloric materials with large magnetic entropy change, low hysteresis, and appropriate magnetic transition temperature. Moreover, this concept of designing heterogeneous structure from the perspective of characteristic cluster and preferential nanocrystalline can be applied to tune other functional properties of MGs.

Declaration of Competing Interest

The authors declare no conflict of interest.

Acknowledgment

We thank Profs. H.J. Lin and Y. Zhang for help in isothermal hydrogenation. This work was supported by the National Natural Science Foundation of China (Grant Nos. 51631003, 51971061 and 11674052).

References

[1] K.A. Gschneidner, V.K. Pecharsky, Annu. Rev. Mater. Sci. 30 (2000) 387–429.
[2] V. Franco, J.S. Blazquez, J.J. Ipus, J.Y. Law, L.M. Moreno-Ramirez, A. Conde, Prog. Mater. Sci. 93 (2018) 112–232.
[3] V.K. Pecharsky, K.A. Gschneidner, Phys. Rev. Lett. 78 (1997) 4494–4497.
[4] F.X. Hu, B.G. Shen, J.R. Sun, Z.H. Cheng, G.H. Rao, X.X. Zhang, Appl. Phys. Lett. 78 (2001) 3675–3677.
[5] Z.S. Xu, Y.T. Dai, Y. Fang, Z.P. Luo, K. Han, C.J. Song, Q.J. Zhai, H.X. Zheng, J. Mater. Sci. Technol. 34 (2018) 1337–1343.
[6] O. Tegus, E. Bruck, K.H.J. Buschow, F.R. de Boer, Nature 415 (2002) 150–152.
[7] L. Zhang, S.C. Ma, Q. Ge, K. Liu, Q.Z. Jiang, X.Q. Han, S. Yang, K. Yu, Z.C. Zhong, J. Mater. Sci. Technol. 33 (2017) 1362–1370.
[8] J. Bai, D. Liu, J.L. Gu, X. Jiang, X.J. Liang, Z.Q. Guan, Y.D. Zhang, C. Esling, X. Zhao, L. Zuo, J. Mater. Sci. Technol. 74 (2021) 46–51.
[9] P. Jia, L.P. Duan, K. Wang, E.G. Wang, J. Mater. Sci. Technol. 35 (2019) 2283–2287.
[10] Q. Luo, W.H. Wang, J. Alloy. Compd. 495 (2010) 209–216.
[11] Y. Zhang, T.T. Zuo, Z. Tang, M.C. Gao, K.A. Dahmen, P.K. Liaw, Z.P. Lu, Prog. Mater. Sci. 61 (2014) 1–93.
[12] L.W. Li, C. Xu, Y. Yuan, S.Q. Zhou, Mater. Res. Lett. 6 (2018) 413–418.
[13] Y.H. Li, S.W. Wang, X.W. Wang, M.L. Yin, W. Zhang, J. Mater. Sci. Technol. 43 (2020) 32–39.
[14] L. Luo, H.X. Shen, Y. Bao, H. Yin, S.D. Jiang, Y.J. Huang, S. Guo, S.Y. Gao, D.W. Xing, Z. Li, J.F. Sun, J. Magn. Magn. Mater. 507 (2020) 166856.
[15] J.T. Kim, S.H. Hong, J.M. Park, J. Eckert, K.B. Kim, J. Mater. Sci. Technol. 43 (2020) 135–143.
[16] L.T. Zhang, Y.J. Duan, T. Wada, H. Kato, J.M. Pelletier, D. Crespo, E. Pineda, J.C. Qiao, J. Mater. Sci. Technol. 83 (2021) 248–255.
[17] J.T. Huo, L.S. Huo, H. Men, X.M. Wang, A. Inoue, J.Q. Wang, C.T. Chang, R.W. Li, Intermetallics 58 (2015) 31–35.
[18] J. Li, L. Xue, W.M. Yang, C.C. Yuan, J.T. Huo, B.L. Shen, Intermetallics 96 (2018) 90–93.
[19] P. Vajda, K.A. Gschneidner, L. Eyring, in: Handbook on the Physics and Chemistry of Rare Earths, 20, North-Holland, Amsterdam, 1995, pp. 207–291.
[20] X.F. Han, L.Y. Lin, T. Miyazaki, F.M. Yang, R.G. Xu, X.H. Wang, H.G. Pan, C.P. Chen, J. Mater. Sci. Technol. 15 (1999) 5–9.
[21] Y.F. Chen, F. Wang, B.G. Shen, F.X. Hu, J.R. Sun, G.J. Wang, Z.H. Cheng, J. Phys. 15 (2003) L161–L167.
[22] A. Fujita, S. Fujieda, Y. Hasegawa, K. Fukamichi, Phys. Rev. B 67 (2003) 104416.
[23] Y.Y. Shao, J. Liu, M.X. Zhang, A.R. Yan, K.P. Skokov, D.Y. Karpenkov, O. Gutfleisch, Acta Mater. 125 (2017) 506–512.
[24] A. Fujita, Acta Mater. 169 (2019) 162–171.
[25] V.B. Chzhan, I.S. Tereshina, E.A. Tereshina-Chitrova, G.S. Burkhanov, G.A. Politova, H. Drulis, J. Magn. Magn. Mater. 470 (2019) 41–45.
[26] H. Sepehri-Amin, I. Dirba, X. Tang, T. Ohkubo, T. Schrefl, O. Gutfleisch, K. Hono, Acta Mater. 175 (2019) 276–285.
[27] B.B. Wang, L.S. Luo, F.Y. Dong, L. Wang, H.Y. Wang, F.X. Wang, L. Luo, B.X. Su, Y.Q. Su, J.J. Guo, H.Z. Fu, J. Mater. Sci. Technol. 45 (2020) 198–206.
[28] H. Fu, M. Zou, N.K. Singh, Appl. Phys. Lett. 97 (2010) 262509.
[29] Q. Zheng, H. Fu, M.X. Wang, Int. J. Mod. Phys. B 26 (2012) 1250041.
[30] Q. Luo, B. Schwarz, N. Mattern, J. Shen, J. Eckert, AIP Adv. 3 (2013) 032134.
[31] T. Hashimoto, T. Numasawa, M. Shino, T. Okada, Cryogenics 21 (1981) 647–653 (Guildf).
[32] L.W. Li, Z. Ding, D.X. Huo, Y.P. Guo, Y. Qi, R. Poettgen, J. Alloy. Compd. 680 (2016) 415–418.
[33] Y.K. Zhang, D. Guo, Y. Yang, J. Wang, S.H. Geng, X. Li, Z.M. Ren, G. Wilde, Intermetallics 88 (2017) 61–64.
[34] L.W. Li, P. Xu, S.K. Ye, Y. Li, G.D. Liu, D.X. Huo, M. Yan, Acta Mater. 194 (2020) 354–365.
[35] H. Oesterreicher, F.T. Parker, J. Appl. Phys. 55 (1984) 4334–4338.
[36] Q. Luo, D.Phuong Nguyen, X. Kou, J. Shen, J. Alloy. Compd. 725 (2017) 835–839.
[37] Q. Luo, B. Schwarz, N. Mattern, J. Eckert, Phys. Rev. B 82 (2010) 024204.
[38] S.K. Banerjee, Phys. Lett. 12 (1964) 16–17.
[39] V. Franco, J.S. Blázquez, A. Conde, Appl. Phys. Lett. 89 (2006) 222512.
[40] V. Franco, A. Conde, Int. J. Refrig. 33 (2010) 465–473.
[41] W.E. Wallace, G. Alefeld, J. Völkl, in: Hydrogen in Metals I, 28, Springer, 1978, pp. 169–195.
[42] C.A.M. Mulder, A.J. Vanduyneveldt, J.A. Mydosh, Phys. Rev. B 25 (1982) 515–518.
[43] A.T. Ogielski, Phys. Rev. B 32 (1985) 7384–7398.
[44] K. Binder, A.P. Young, Rev. Mod. Phys. 58 (1986) 801–976.
[45] L. Xue, L.L. Shao, Q. Luo, L.N. Hu, Y.B. Zhao, K.B. Yin, M.Y. Zhu, L.T. Sun, B.L. Shen, X.F. Bian, J. Mater. Sci. Technol. 77 (2021) 28–37.
[46] L.L. Shao, Q.Q. Wang, L. Xue, M.Y. Zhu, A.D. Wang, J.H. Luan, K.B. Yin, Q. Luo, Q.S. Zeng, L.T. Sun, B.L. Shen, J. Mater. Res. Technol. 11 (2021) 378–391.
[47] Q. Wang, C.T. Liu, Y. Yang, J.B. Liu, Y.D. Dong, J. Lu, Sci. Rep. 4 (2014) 4648.
[48] D. Granata, E. Fischer, J.F. Loeffler, Scr. Mater. 103 (2015) 53–56.
[49] L. Xia, Q. Guan, D. Ding, M.B. Tang, Y.D. Dong, Appl. Phys. Lett. 105 (2014) 192402.